

SCIENTIFIC REPORTS

OPEN

Thermal hysteresis measurement of the VO₂ emissivity and its application in thermal rectification

C. L. Gomez-Heredia^{1,2}, J. A. Ramirez-Rincon^{1,2}, J. Ordonez-Miranda^{1,2}, O. Ares¹, J. J. Alvarado-Gil^{1,2}, C. Champeaux³, F. Dumas-Bouchiat³, Y. Ezzahri^{1,2} & K. Joulain²

Hysteresis loops in the emissivity of VO₂ thin films grown on sapphire and silicon substrates by a pulsed laser deposition process are experimentally measured through the thermal-wave resonant cavity technique. Remarkable variations of about 43% are observed in the emissivity of both VO₂ films, within their insulator-to-metal and metal-to-insulator transitions. It is shown that: i) The principal hysteresis width (maximum slope) in the VO₂ emissivity of the VO₂ + silicon sample is around 3 times higher (lower) than the corresponding one of the VO₂ + sapphire sample. VO₂ synthesized on silicon thus exhibits a wider principal hysteresis loop with slower MIT than VO₂ on sapphire, as a result of the significant differences on the VO₂ film microstructures induced by the silicon or sapphire substrates. ii) The hysteresis width along with the rate of change of the VO₂ emissivity in a VO₂ + substrate sample can be tuned with its secondary hysteresis loop. iii) VO₂ samples can be used to build a radiative thermal diode able to operate with a rectification factor as high as 87%, when the temperature difference of its two terminals is around 17 °C. This record-breaking rectification constitutes the highest one reported in literature, for a relatively small temperature change of diode terminals.

The capability of manipulating heat to control and process information via phonons, photons, and electrons is of critical importance to efficiently manage the energy resources of nature¹. Inspired by the ability of the electronic diode to rectify electrical currents, different models of thermal diodes have been conceived and theorized over the last decade. The working principle of this thermal device is based on the asymmetry of the heat flux exchanged between its two terminals when their temperature difference is reversed². This thermal asymmetry is usually characterized by the rectification factor $R = |q_F - q_B| / \max(q_F, q_B)$, where q_F and q_B stand for the magnitudes of the heat fluxes in the forward and the backward configurations, respectively, for a given temperature difference between the thermal diode terminals. The rectification of conductive heat fluxes is the result of the nonlinearity in the phonon^{3–8} and electron^{9,10} heat channels and was experimentally observed with $R > 20\%$ in carbon and boron nanotubes¹¹, semiconductor quantum dots¹², nanoribbons^{3,13}, reduced graphene oxide¹⁴ and bulk cobalt oxides¹⁵.

Thermal rectification through photons driving radiative heat fluxes in both the far^{16–18} and near^{19–21} fields has also been studied widely. Far-field radiative thermal diodes, involving terminals of selective emitters¹⁶ and superconducting materials¹⁷ operating with rectification factors up to 70% have been proposed for a temperature difference of 200 K between terminals. In the near-field regime, on the other hand, Iizuka and Fan¹⁹ found a rectification factor $R = 44\%$, for a thermal diode with terminals of coated and uncoated SiC at temperatures of 500 K and 300 K, respectively. These values of the rectification factor in the far and near fields are determined by the terminals permittivity and they have been enhanced up to 90% in radiative thermal diodes capitalizing on the strong permittivity contrast of vanadium dioxide (VO₂)^{22–24}. This phase-change material (PCM), with a strongly correlated electron system, is thus very promising for controlling heat currents due to its reversible metal-insulator transition (MIT) with thermal hysteresis in a small temperature range near room temperature. Below 341 K, VO₂ exhibits an insulating monoclinic phase that becomes a metallic rutile one above ~ 346 K^{25,26}, which induces sizeable changes on its electrical, optical, and thermal properties. These changes on the VO₂ properties have allowed the development of models for radiative thermal transistors^{27–31}, thermal memories³², microwave switches^{33,34}, etc.

¹Departamento de Física Aplicada, Cinvestav-Unidad Mérida, Carretera Antigua a Progreso km. 6, 97310, Mérida, Yucatán, Mexico. ²Institut Pprime, CNRS, Université de Poitiers, ISAE-ENSMA, F-86962, Futuroscope Chasseneuil, France. ³Université de Limoges, CNRS, IRCER, UMR 7315, F-87000, Limoges, France. Correspondence and requests for materials should be addressed to J.O.-M. (email: jose.ordonez@cnrs.pprime.fr)

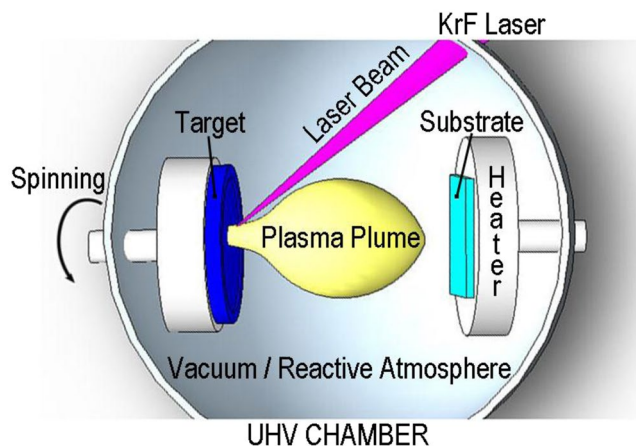


Figure 1. Scheme of the working principle of the pulsed laser deposition (PLD) process.

The aspiration of applying VO₂ in devices with optimal performances has led to a progressive study and tailoring of the VO₂ physical properties through its MIT. Several works on the electrical resistivity^{35–39} and electrical conductivity⁴⁰ of single crystals and thin films of VO₂, reported variations of four and five orders of magnitude, respectively. Yang *et al.*³⁹ showed that the width of the hysteresis loop of the VO₂ electrical resistivity, sharpness of the transition, and transition temperature, depend strongly on the epitaxial growth of VO₂ films on sapphire. This indicates that the substrate, as well as the growth process used, represent an effective way to tailor the overall properties of VO₂ films. On the other hand, thermal conductivity variations of VO₂ films as large as 60% were measured by ultrafast pump-probe techniques^{41,42}. The optical transmittance, reflectance, and absorption of VO₂ films were also measured within its MIT⁴³, such that very high absorptions (~99.75%) were observed for film thicknesses even smaller than the incident wavelength $\lambda = 11.6\ \mu\text{m}$. Furthermore, the VO₂ emissivity was measured indirectly, inside⁴⁴ and outside⁴⁵ the MIT, by means of infrared transmittance and reflectance measurements. Leahu *et al.*⁴⁶ quantified an emissivity hysteresis of about 8 K for a VO₂ thin film deposited on a silicon wafer and showed that the emissivity variations determined through reflectance measurements in the spectral range (2.5–5.0) μm and on the side of the Si wafer ($\Delta\epsilon = 0.47$) are twice larger than those on the VO₂ side. In addition, these latter authors also observed an anomalous absorption phenomenon through the presence of an emissivity maximum during the heating and cooling processes of VO₂. The effects of the film thickness, substrate material, and multi-layer structures, on the emissivity of the VO₂ films have also been studied indirectly^{47–50}. Given that these indirect measurements of the VO₂ emissivity require the a priori knowledge of other optical parameters, it is desirable to measure it by means of more accurate experimental methodologies, that allow a deeper comprehension of the involved phenomena occurring during the MIT.

In this paper, we directly measure the principal and secondary hysteresis loops of the VO₂ emissivity during the heating and cooling processes around its MIT. This is done through the thermal-wave resonant cavity technique (TWRC), for two types of VO₂ thin films deposited on r-sapphire and silicon (100) substrates by means of the pulsed laser deposition (PLD) process. We show that the substrate has a significant impact on the growth of the VO₂ thin films and therefore on their overall emissivity, such that the sample with the silicon substrate yields slower MITs and wider hysteresis loops than the one deposited on sapphire. Furthermore, we find that the width along with the rate of change of the VO₂ emissivity can be tuned through secondary hysteresis loops. Finally, the experimental values of the VO₂ emissivity are applied to theoretically assess the rectification factor of a radiative thermal diode based on VO₂.

Methods and Materials

Sample fabrication. Vanadium dioxide thin films have been deposited over substrates of r-sapphire and silicon (100) wafers through the PLD process. This well-adapted method for the deposition of complex multi-element materials and oxides consists in using a pulsed high-power laser beam to evaporate a small amount of matter from a solid target within a stainless-steel ultra-high vacuum chamber, as shown in Fig. 1. After some hundreds or thousands of laser pulses, the evaporated matter condensed on a substrate forms a thin film. A KrF pulsed excimer laser with wavelength $\lambda = 248\ \text{nm}$, pulse width of 25 ns, and repetition rate of 25 Hz has been employed to grow VO₂ films on r-sapphire and silicon (100) substrates set at the temperature of 600 °C. The oxygen pressure used for the deposition of all samples has been of 2.2 Pa. The main characteristics of the substrates and VO₂ thin films are summarized in Table 1.

Sample characterization. The crystalline structure of our VO₂ samples has been analyzed by X-Ray Diffraction (XRD), whose patterns are shown in Fig. 2. The XRD pattern of sample 1 has been determined through a diffractometer D-8 Advance working with a Bragg-Brentano geometry and CuK_{α1} radiation (Fig. 2a), while that of sample 2 (Fig. 2b) has been found by using a diffractometer Siemens D-5000 ($\theta, 2\theta$) operating with an small angle and CuK_{α2} radiation, due to the relatively high intensity of its peaks. According to the International Centre for Diffraction Data (Card 04–003–2035), the data of both samples are found to be consistent with the monoclinic phase of VO₂ (red lines in Fig. 2), as expected. The VO₂ film deposited on r-sapphire (Fig. 2a) presents

	Sample 1	Sample 2
Substrate	r-sapphire	silicon (100)
Dopant and doping concentration	—	P-type: Boron 7×10^{14} to 1×10^{16} at/cm ³
Substrate thickness L1 (μm)	510	525
VO ₂ thin film thickness L2 (nm) ^a	120	300
Emissivity (at room temperature) ^b , ϵ_{1amb}	0.59	0.52

Table 1. Main characteristics about the substrates and VO₂ film properties. ^aMeasured by profilometry (KLA-Tencor AlphaStep D-120), ^bDetermined by a PerkinElmer Frontier FTIR spectrometer in the wavelength range of 2–22 μm , as detailed in the supplementary material.

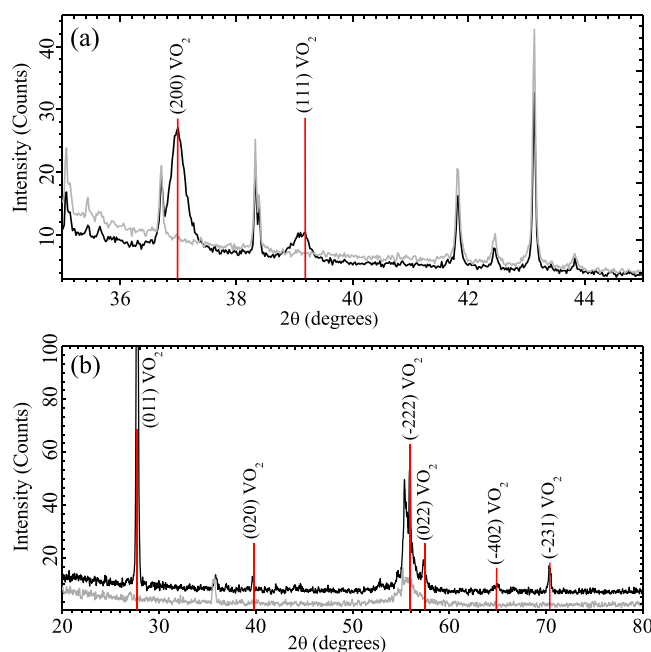


Figure 2. (Black line) Room temperature XRD patterns of VO₂ films grown on (a) r-sapphire (sample 1) and (b) silicon 100 (sample 2). Gray lines stand for XRD patterns of the substrates.

an orientation at the (200) and (111) diffraction peaks, while the one deposited on silicon (Fig. 2b) is not oriented and shows a principal peak in the plane (011).

The structural characterization of the samples' surface has been performed by Field Emission Scanning Electron Microscope (FESEM JEOL 7600 F). The images obtained for the samples 1 and 2 are respectively shown in Fig. 3(a,b), which show that the grains formed on the r-sapphire substrate exhibit spherical-like and elongated shapes, such that they are well interconnected in a columnar growth. On the other hand, the grains formed on silicon present pyramidal, cubic, and sharp shapes with a connectivity relatively weaker than those on r-sapphire. These results are consistent with those obtained by an Atomic Force Microscope (AFM) integrated to a Confocal Raman Witec Alpha300 spectrometer, as shown in Fig. 3(c,d). The three-dimensional AFM plots of a $2 \times 2 \mu\text{m}^2$ are presented in Fig. 3(e,f) for both samples. The grain sizes in sample 1 varies within the range (0.12; 0.40) μm , while those in sample 2 are in the interval (0.20; 0.26) μm . In addition, the surface roughness of sample 1 (13.1 nm) and sample 2 (5.2 nm) have been obtained from the arithmetical mean height (5.14 nm, 14.2 nm), the root mean square height (7.2 nm, 15.7 nm) and the maximum height (28.6 nm, 106.5 nm). These morphological differences of the samples 1 and 2 are expected to have a direct impact on the effective emissivity of our VO₂ films, as reported in Table 2.

Experimental setup. The experimental setup used to measure the emissivity of our VO₂ thin films consists of a thermal-wave resonant cavity (TWRC) implemented with a heating and data acquisition equipment, as shown in Fig. 4(a). The working principle of this standard photothermal technique is based on the detection of periodic temperature fluctuations (thermal waves) generated by a thin film (heater) in response to the absorption of a modulated light beam, and then transmitted through an intra-cavity fluid of thickness L towards a sensor placed parallel to the heater (Fig. 4(b))⁵¹. As the heat transport within this cavity involves both heat conduction^{52,53} and radiation^{54–56}, the TWRC was applied to accurately determine the thermal diffusivity of fluids^{57–60} as well as the emissivity of solid thin films⁵⁶ and selective solar coatings⁶¹. In our experimental setup, the intra-cavity fluid is air, the heat emitter is the VO₂ + substrate sample (1.0 cm in diameter) that is heated by an infrared diode laser beam (100 mW, $\lambda = 808$ nm), whose spot uniformly covers all the heater and its intensity is

	Sample 1 (120 nm) VO ₂ + r-sapphire	Sample 2 (300 nm) VO ₂ + silicon 100	Sample 3 (300 nm) VO ₂ + r-sapphire	Sample 4 (130 nm) VO ₂ + silicon 100
Emissivity change ($\Delta\epsilon_i$)	0.45	0.42	0.34	0.27
Critical temperature (T_c)	64.4°C	64.3°C	61.2°C	65.8°C
Width of main hysteresis (ΔH)	3.3°C	10.8°C	2.2°C	13.7°C
Slope of the MIT [$\beta = -(\partial\epsilon_i/\partial T_i)_{T_i=T_c}$]	0.08/°C (†)	0.03/°C (†)	0.07/°C (†)	0.01/°C (†)

Table 2. MIT characteristics in the emissivity of VO₂ films grown on a sapphire (sample 1) and silicon (sample 2) substrate. Vertical arrows, for the slope β , stand for the heating process.

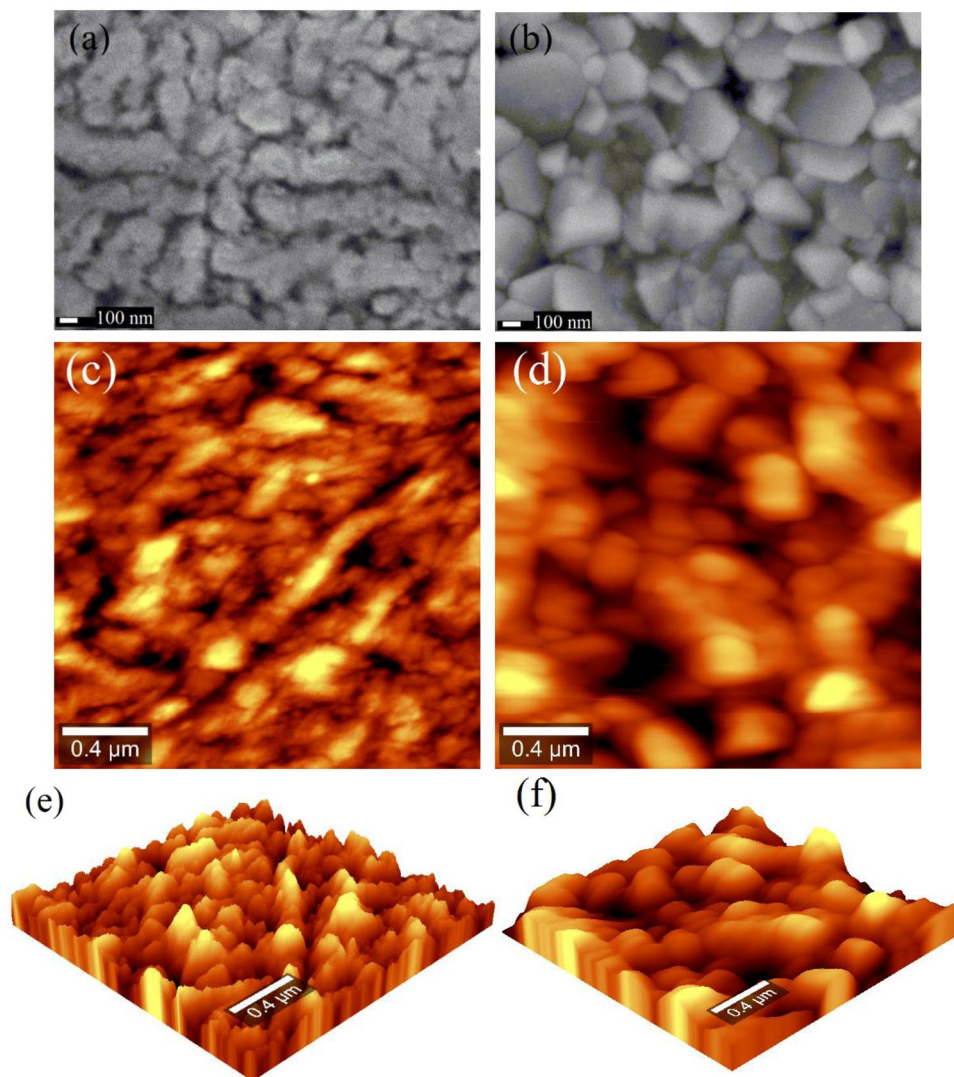


Figure 3. SEM micrograph of (a) sample 1: VO₂ (120 nm) + r-sapphire and (b) sample 2: VO₂ (300 nm) + silicon 100. Two and three-dimensional AFM images of (c–e) sample 1 and (d–f) sample 2.

modulated with a frequency $f = 3$ Hz. At this modulation frequency, the signal-to-noise ratio is high, even when the sample temperature increases through values within the MIT of VO₂. The temperature of the VO₂ + substrate sample during its heating and cooling is controlled with a Peltier cell ($V_{\max} = 5.3$ V, $I_{\max} = 5.7$ A, $\Delta T_{\max} = 68$ °C) that has a center hole allowing the incidence of the laser beam onto the sample (Fig. 2(b)). The voltage applied to the Peltier cell is switched in 0.1 V every 5 minutes, which leads to changes of about 1.7 °C in the temperature of the sample. The amplitude and phase delay of the TWRC signal are detected through a PZT pyroelectric ceramic sensor covered by a black thin layer of average absorbance 0.85 in the spectral wavelength range between 2–15 μm , positioned in front of the emitter. The pyroelectric voltage signal is fed into a preamplifier (Stanford Research Systems SR-560) and then sent into the lock-in amplifier (Stanford Research Systems SR-830 DSP) for further amplification, filtering, and demodulation. The reported signals correspond to an average of five repetitions for

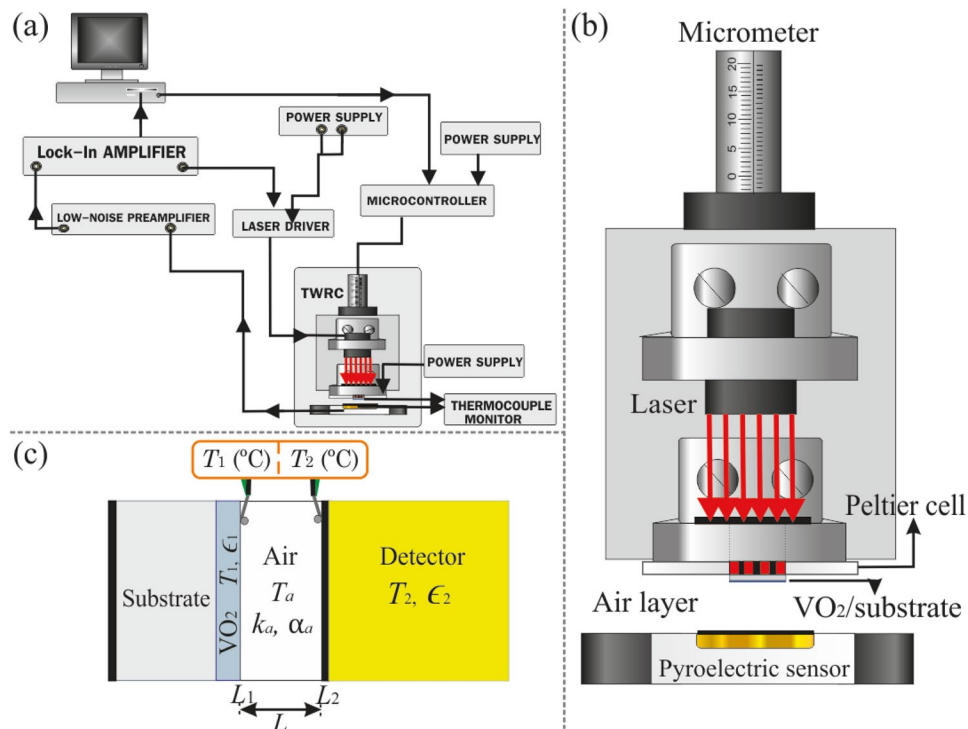


Figure 4. Scheme of the (a) experimental setup along with a (b) zoom-in on the resonant cavity used to monitor the photothermal signal. (c) Schematic illustration of the layered system undergoing heat transport.

each fixed temperature. The cavity length $L = 3.5$ mm is set with a micrometer coupled with a stepper motor (resolution of $10\ \mu\text{m}$), while the temperatures of the sample (T_1) and sensor (T_2) surfaces are measured by means of K-thermocouples (0.05 mm in diameter) placed as shown in Fig. 4(c) and a thermocouple monitor (2-Channel Handheld Digital Thermometer) with $0.1\ \text{°C}$ of resolution.

Theoretical model. Taking into account the laser spot, modulation frequency, and cavity length used in our experimental setup, the heat propagation inside the heater ($\text{VO}_2 + \text{substrate}$) and air layer, shown in Fig. 4(c), can be considered as predominantly one-dimensional. Under this condition, the normalized photothermal signal V recorded by the detector is given by⁵³:

$$V(f, L, T_1, \epsilon_1) = \frac{k_a}{e_1 L_1 \sqrt{2\pi f}} \frac{\sqrt{\alpha_1}}{\sqrt{\alpha_a}} \left(\frac{1}{\sqrt{i} \sinh(\sigma_a L)} - i \frac{\epsilon}{\epsilon_0} \right) \quad (1)$$

where L_1 , e_1 and α_1 are the thickness, thermal effusivity, and thermal diffusivity of the heater, respectively; $\sigma_a = (1 + i)/\mu_a$, $\epsilon_0 = e_a \sqrt{2\pi f} / (4\sigma T_1^3)$, $\mu_a = \sqrt{\alpha_a / \pi f}$, α_a , k_a and e_a are the respective thermal diffusivity, thermal conductivity, and thermal effusivity of the air layer, $\epsilon = (\epsilon_1^{-1} + \epsilon_2^{-1} - 1)^{-1}$, with ϵ_1 and ϵ_2 being the emissivity of the heater and the sensor, respectively, and σ is the Stefan-Boltzmann constant. The experimental values of the amplitude and phase of V have been used to determine the emissivity ϵ_1 of our VO_2 thin films at different temperatures within their MITs.

Results and Discussion

The amplitude and phase measured for the $\text{VO}_2 + \text{sapphire}$ and pure sapphire samples are shown in Fig. 5(a,b), respectively. Note that both signals vary linearly with the sapphire temperature during the heating and cooling processes, such that their corresponding values agree with those obtained for the $\text{VO}_2 + \text{sapphire}$ sample at low temperatures out of its MIT. This agreement indicates that, for these temperatures, the photothermal signals are mainly governed by the substrate and therefore no VO_2 thin film information can be extracted from them. This confirms the fact that for such nanometric thickness, VO_2 is fairly transparent to the infrared radiation in the dielectric phase⁶². Furthermore, during the heating process of sapphire, the amplitude takes higher values than for the cooling one, while the phase values are practically the same for both processes. The linear dependence between the temperatures of the sensor (T_2) and sample (T_1), with a slope for the heating process that is higher than the one for the cooling process (Fig. 6), indicates that the linear temperature dependence of the signals shown in Fig. 5 is due to the variations of T_2 , while the dependence (independence) of the amplitude (phase) on the heating and cooling process is due to its high (low) sensitive to the thermal energy stored by the sensor. To eliminate the dependence of the amplitude and phase on T_2 , and therefore on the effect of the Peltier heater, their values obtained for the $\text{VO}_2 + \text{substrate}$ sample are going to be normalized with the corresponding ones recorded for the substrate alone, under the same experimental conditions. The normalized signals thus obtained have the

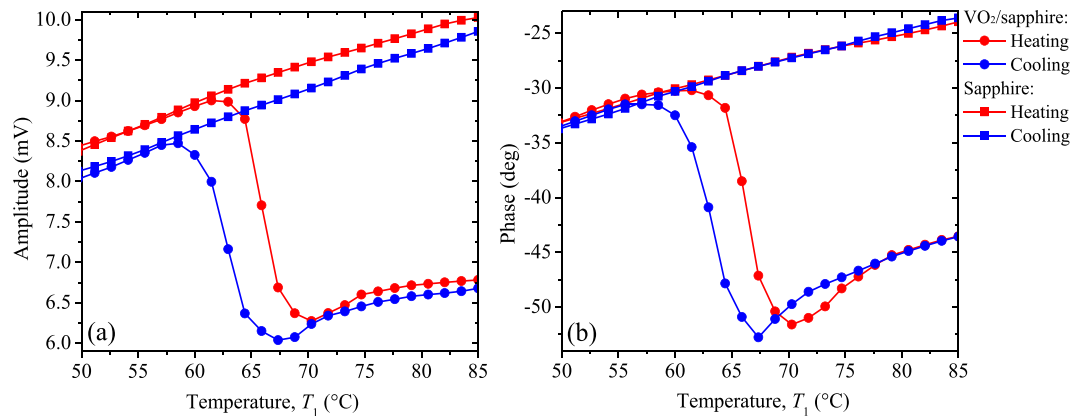


Figure 5. (a) Amplitude and (b) phase signals measured for the VO₂ + sapphire sample (circles) and the sapphire substrate (squares) during the heating (red) and cooling (blue) processes.

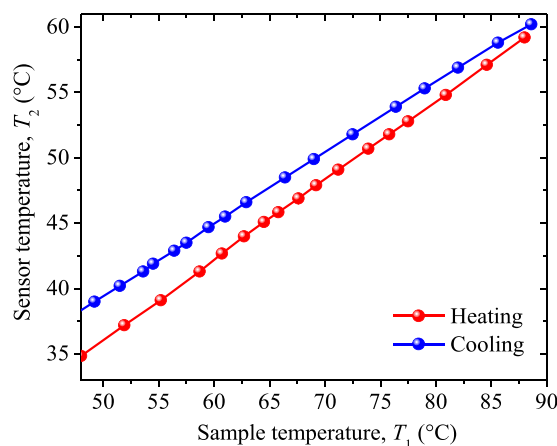


Figure 6. Sensor temperature as a function of the sample one, for the heating (red) and cooling (blue) processes.

advantage of being independent of the substrate thermal properties (Eq. 1) and therefore their changes can be properly used to determine the temperature variations of the effective emissivity of the VO₂ + substrate system, once its room temperature value is known (Table 1) and the thermal properties (k_a, α_a) of the intra-cavity air layer are determined from the kinetic theory of gases, for the average temperature $(T_1 + T_2)/2$. In addition, outside of the MIT, this normalization method yields photothermal signals independent of T_1 , as expected (Fig. 7).

The normalized amplitude (NA) and normalized phase (NP) obtained for the sample 1 (VO₂ + sapphire) are respectively shown in Fig. 7(a,b), as functions of its temperature T_1 , during the heating and cooling processes around the MIT. Within this MIT, both the NA and NP depend strongly on T_1 and take different values for the heating and cooling processes, which shows that they are sensitive to the thermal hysteresis of our VO₂ sample. The disappearance of this dependence for low and high temperatures, indicates that the sample has reached its dielectric and metallic states, respectively. The significant differences of the NA and NP between these states are of 34% and 24.4 degrees, respectively, and involve a characteristic hysteresis cycle on both signals. A similar behavior is exhibited by the NA and NP shown in Fig. 8(a,b) for the sample 2 (VO₂ + silicon), however, the hysteresis width (11.5°C) at mid height of the normalized amplitude, for this latter sample, is significantly wider than that (3.3°C) of the former one. These sizeable differences on the hysteresis width also show up on the normalized phase and are reasonable due to the fact that the VO₂ film growth orientation along with the shape and distribution of the film grains, are mainly driven by the substrate material, as shown in Figs 2 and 3 as well as in the supplementary material. The silicon substrate of VO₂ films thus enables an epitaxial growth and microstructure that generate a wider thermal hysteresis than sapphire.

Figure 9(a,b) show the emissivity ϵ_1 of our VO₂ thin films deposited on a substrate of sapphire (sample 1) and silicon (sample 2), respectively. In the MIT, ϵ_1 decreases during the heating process and increases for the cooling one, following a different path, which leads to a hysteresis loop similar to that of its corresponding photothermal signals shown in Figs 7 and 8. The significant variations of ϵ_1 from 0.59 (0.52) in the insulating phase, to 0.13 (0.10) in the metallic one, of sample 1 (2), are consistent with previous results reported in the literature for VO₂ thin films grown on a sapphire^{30,31,44} (silicon)^{45–48} substrate. However, in contrast to these seven-latter works based on conventional reflectance/transmittance spectroscopy operating in a limited spectral range (2–15 μm),

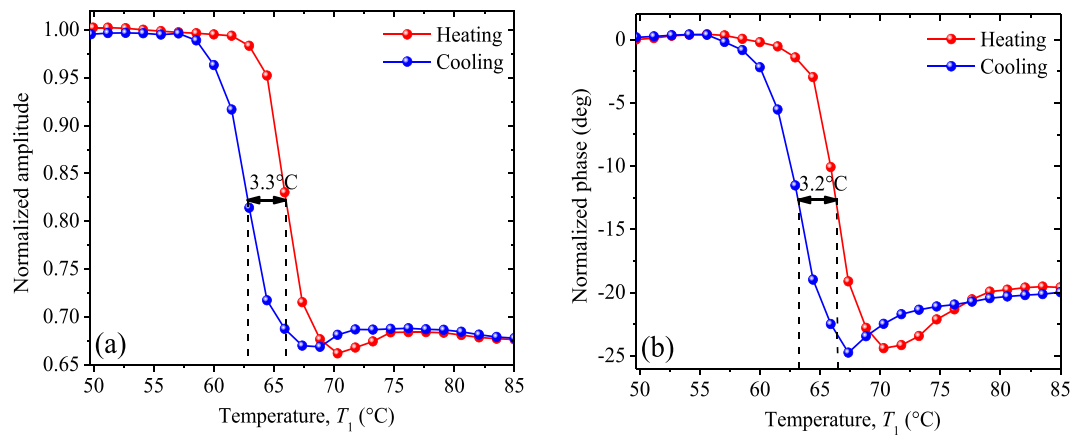


Figure 7. (a) Normalized amplitude and (b) normalized phase obtained during the heating and cooling of sample 1, as functions of its temperature within its MIT.

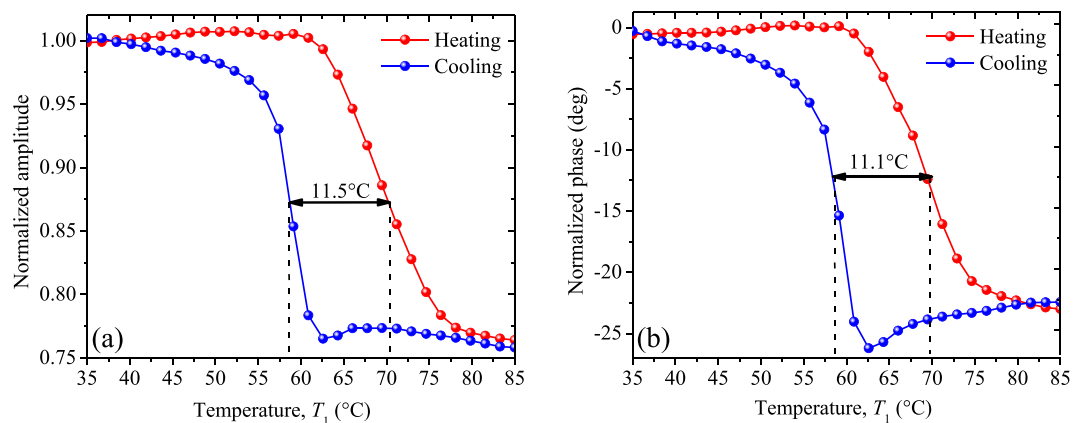


Figure 8. (a) Normalized amplitude and (b) normalized phase obtained during the heating and cooling of sample 2, as functions of its temperature within its MIT.

our direct measurements of the VO_2 emissivity ϵ_1 are expected to be more accurate, as the thermal-wave resonant cavity is able to detect radiation in a much broader spectra range. The effect of the MIT on the emissivity of each sample can be characterized by the emissivity change $\Delta\epsilon_1$, critical temperature of transition (T_c), width (ΔH), and slope (β); which are summarized in Table 2. Note that samples 1 and 2 have similar values for $\Delta\epsilon_1$ and T_c , but sizeable differences on ΔH and β . Sample 2 exhibits a parameter ΔH (β) around 3 times greater (smaller) than that of sample 1. These differences can be attributed to the growth orientation and the surface morphology of our VO_2 thin films, which depend on their respective substrate^{39,48–50} and film thickness^{47,50}, as shown in Figs 2 and 3. Taking into account that the thin films deposited by the PLD technique can be considered as a collection of grains (Fig. 3), which in the VO_2 /sapphire sample exhibit a stronger coupling than in the VO_2 /silicon, and that a crystal requires less energy to change its phase when their grains are more coupled, the ΔH (β) of this latter sample should be wider (slower) than that of the former one, as reported in Table 2. Note that Table 2 also shows that the width ΔH and slope β of the emissivity of samples with the same substrate (samples 1 and 3 or samples 2 and 4) do not change significantly with the sample thickness, which confirms that the values of these parameters are mainly determined by the substrate. This fact is further supported by Figs 3 and S7, which show that the film substrate has a stronger impact than the film thickness, on the shape and distribution of grains. It is therefore clear that a silicon substrate yields wider hysteresis loops with slower phase transition rates than sapphire. This result may be used, for instance, in optical memory-type applications, which require a large ΔH ⁶³, and for the development of VO_2 -based bolometers, in which a small ΔH is preferable⁶⁴.

Secondary hysteresis loops (2, 3), shown in Fig. 9(a,b), have been obtained by interrupting the heating process of both samples at a temperature T_f within their MITs. These mini loops span inside the principal ones (1), especially for sample 2, which has a wider hysteresis loop (1) than sample 1. Note that the cooling branches of the three loops recorded for sample 2 follow different paths, such that they reach the insulating-state emissivity at different temperatures T_{oi} (Fig. 9(b)). Lower T_f generates a hysteresis loop with higher T_{oi} and therefore smaller ΔH . Given that the slope β of the emissivity also decreases as T_f (or ΔH) reduces, during the cooling process, the hysteresis width, transition rate, and variation of the VO_2 emissivity can be cut off by interrupting the heating process at a low enough T_f . On the other hand, note that the minimum of the principal hysteresis loop of sample 2 also

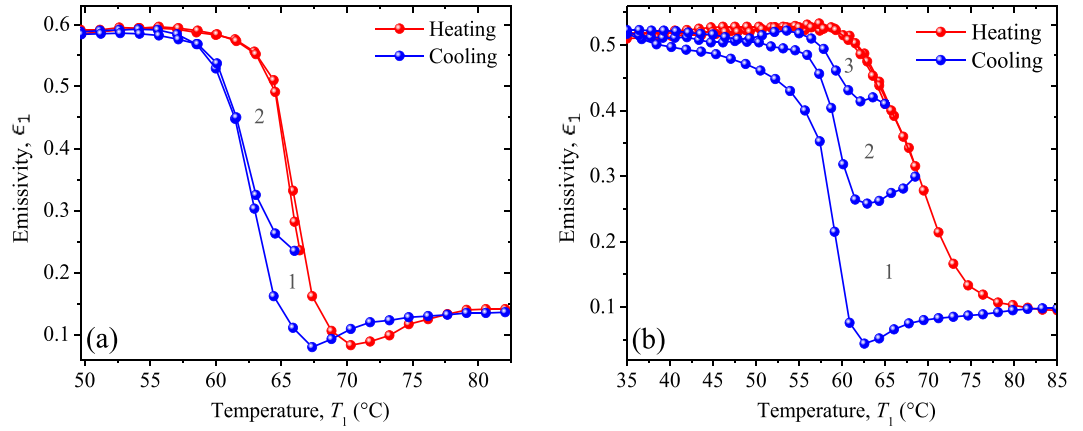


Figure 9. Principal (1) and secondary (2, 3) hysteresis loops of the emissivity of VO₂ thin films grown on (a) r-sapphire and (b) silicon (100) substrates.

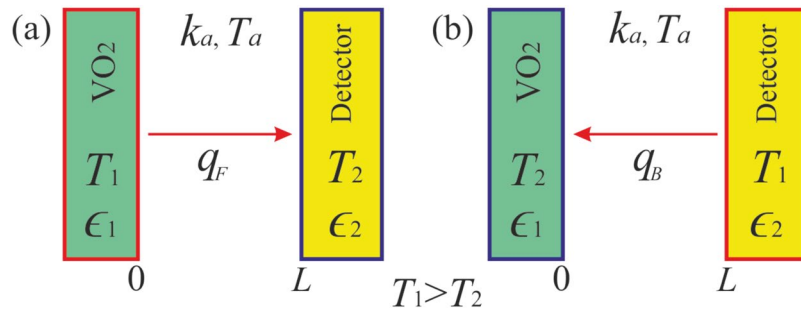


Figure 10. Scheme of a thermal diode operating in the (a) forward and (b) backward configurations.

shows up on their secondary ones, but tends to disappear as VO₂ moves away from its metallic state (lower T_f). These minima are consistent with previous observations⁴⁶ and can be associated to the anomalous energy absorption of VO₂.

Application in thermal rectification. The experimental variations of the VO₂ emissivity $\epsilon_1(T)$ with temperature are now applied to assess the rectification factor of the radiative thermal diode operating in the forward and backward configurations shown in Fig. 10(a,b). This diode essentially consists of a TWRC (Fig. 4(c)), whose terminals are set at temperatures T_1 and T_2 ($T_2 < T_1$) and are separated by an air layer of thermal conductivity $k_a(T_a)$, with $T_a = (T_1 + T_2)/2$. Taking into account the conductive heat flux $q_C = k_a(T_1 - T_2)/L$ propagating through the air between the diode terminals, the net heat flux in the forward (q_F) and backward (q_B) bias are given by

$$q_F = \frac{k_a}{L}(T_1 - T_2) + \epsilon(T_1)\sigma(T_1^4 - T_2^4), \tag{2a}$$

$$q_B = \frac{k_a}{L}(T_1 - T_2) + \epsilon(T_2)\sigma(T_1^4 - T_2^4), \tag{2b}$$

where $\epsilon(T) = (\epsilon_1^{-1}(T) + \epsilon_2^{-1} - 1)^{-1}$. For the sake of simplicity, we are going to consider that the detector has a temperature independent emissivity $\epsilon_2 = 0.85$, which is the case of the detector used to perform our experiments (Fig. 4(c)).

According to Fig. 9(a,b), the emissivity $\epsilon_1(T_1) < \epsilon_1(T_2)$ for most temperatures $T_1 > T_2$, which indicates $q_B > q_F$. The rectification factor $R = 1 - q_F/q_B$ can then be written as follows:

$$R = \frac{1}{1 + N} \left(1 - \frac{\epsilon_1(T_1)}{\epsilon_1(T_2)} \right), \tag{3a}$$

$$N = \frac{k_a}{\sigma L} \frac{1}{\epsilon_1(T_2)(T_1 + T_2)(T_1^2 + T_2^2)} \tag{3b}$$

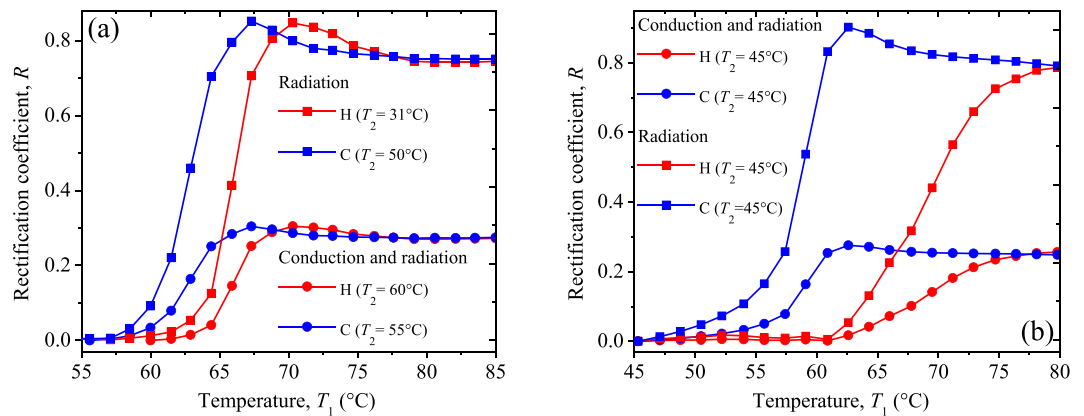


Figure 11. Rectification factor R as a function of the temperature T_1 of a thermal diode made up with a terminal of VO_2 present in (a) sample 1 and (b) sample 2. Calculations have been done for pure radiation (squares) and radiation + conduction (circles) heat transfer, by choosing the temperature T_2 that maximizes R during the heating and cooling processes. The letters H and C stands for the heating and cooling processes, respectively.

Equations (3a) and (3b) establish that, in absence of heat conduction ($k_a = 0$), $N = 0$ and $R = R_{\max} = 1 - \epsilon_1(T_m)/\epsilon_1(T_i)$ takes its maximum value, when the terminal temperatures T_1 and T_2 are chosen as the minimal (T_m) and maximal (T_i) ones supporting the metallic and insulator phases, respectively. By contrast, in presence of heat conduction ($k_a > 0$), the maximum rectification is reached for $T_2 = T_i$ and $T_1 \gg T_m$.

Figure 11(a,b) show the rectification factor R as a function of the temperature T_1 of the thermal diode (Fig. 10) operating with a VO_2 terminal made up of sample 1 or sample 2, respectively. The general increase of R with T_1 , within the MIT of both samples, is the result of the decrease of ϵ_1 when their temperatures rise, as shown in Fig. 9(a,b). In all cases, higher rectifications are obtained when the temperature T_1 (T_2) of the hotter (cooler) diode terminal is chosen in the metallic (insulating) phase of VO_2 , as expected. In this case, the asymptotic value of the rectification factor R of a thermal diode in vacuum (no heat conduction) is 0.73, for sample 1 and 0.78 for sample 2. By contrast, in presence of heat conduction, these values reduce to about 0.26 for both samples. This reduction is reasonable, given that the asymmetry between the heat fluxes q_F and q_B is only driven by the temperature dependence of the VO_2 emissivity and not by the heat conduction through air, as established by Eqs (3a) and (3b). In presence of pure heat radiation, the highest rectification factor $R = 0.87$ occurs at the temperature T_1 for which the VO_2 emissivity exhibits a minimum and is reached for a temperature difference $\Delta T = T_1 - T_2 = 17.3$ °C, in both samples. This record-breaking rectification factor, for a relatively small temperature change of the diode terminals, shows the high suitability of VO_2 for developing efficient radiative thermal diodes.

Conclusions

We have experimentally measured the principal and secondary hysteresis loops of the emissivity of two VO_2 thin films grown on r-sapphire and silicon (100) substrates. These first-time-ever direct measurements have been performed through the high-accurate technique of the thermal-wave resonant cavity, which involves both thermal radiation and heat conduction. Remarkable VO_2 emissivity variations up to 43% have been observed at the extremes of the metal-insulator transition of both VO_2 films. Based on a PLD process, it has been shown that the silicon substrate induces the growth of VO_2 films with three-time slower phase transitions and wider principal hysteresis loops than a sapphire one. We have also found that the hysteresis width and the transition rate of the VO_2 emissivity can be tuned by means of the secondary hysteresis loops. Furthermore, the potential of VO_2 for building up a radiative thermal diode with a record-breaking rectification factor up to 87%, with a relatively small temperature difference of 17.3 °C between its terminals, has been demonstrated.

References

- Wang, L. & Li, B. Phononics gets hot. *Phys. World*, **21**, 27–29 (2008).
- Li, N. *et al.* Colloquium: Phononics: Manipulating heat flow with electronic analogs and beyond. *Rev. Mod. Phys.* **84**, 1045 (2012).
- Li, B. *et al.* Thermal diode: Rectification of heat flux. *Phys. Rev. Lett.* **93**, 184301 (2004).
- Terraneo, M. *et al.* Controlling the energy flow in nonlinear lattices: a model for a thermal rectifier. *Phys. Rev. Lett.* **88**, 094302 (2002).
- Hu, J. *et al.* Thermal conductivity and thermal rectification in graphene nanoribbons: a molecular dynamics study. *Nano Lett.* **9**, 2730–2735 (2009).
- Zhang, G. & Zhang, H. Thermal conduction and rectification in few-layer graphene Y junctions. *Nanoscale* **3**, 4604–4607 (2011).
- Roberts, N. & Walker, D. A review of thermal rectification observations and models in solid materials. *Int. J. Therm. Sci.* **50**, 648–662 (2011).
- Garcia-Garcia, K. & Alvarez-Quintana, J. Thermal rectification assisted by lattice transitions. *Int. J. Therm. Sci.* **81**, 76–83 (2014).
- Nakayama, R. & Takeuchi, T. Thermal rectification in bulk material through unusual behavior of electron thermal conductivity of Al-Cu-Fe icosahedral quasicrystal. *J. Electron. Mater.* **44**(1), 356–361 (2015).
- Segal, D. Single mode heat rectifier: Controlling energy flow between electronic conductors. *Phys. Rev. Lett.* **100**, 105901 (2008).
- Tian, H. *et al.* A novel solid-state thermal rectifier based on reduced graphene oxide. *Sci. Rep.* **2**, 523 (2012).

12. Scheibner, R. *et al.* Quantum dot as thermal rectifier. *New J. Phys.* **10**, 083016 (2008).
13. Yang, N. *et al.* Thermal rectification in asymmetric graphene ribbons. *Appl. Phys. Lett.* **95**, 033107 (2009).
14. Chang, C. W. *et al.* Solid-state thermal rectifier. *Science*. **314**, 1121–1124 (2006).
15. Kobayashi, W. *et al.* An oxide thermal rectifier. *Appl. Phys. Lett.* **95**, 171905 (2009).
16. Nefzaoui, E. *et al.* Simple far-field radiative thermal rectifier using Fabry–Perot cavities based infrared selective emitters. *Appl. Opt.* **53**, 3479–3485 (2014).
17. Nefzaoui, E. *et al.* Radiative thermal rectification using superconducting materials. *Appl. Phys. Lett.* **104**, 103905 (2014).
18. Otey, C. R. *et al.* Thermal rectification through vacuum. *Phys. Rev. Lett.* **104**, 154301 (2010).
19. Iizuka, H. & Fan, S. J. Rectification of evanescent heat transfer between dielectric-coated and uncoated silicon carbide plates. *Appl. Phys.* **112**, 024304 (2012).
20. Basu, S. & Francoeur, M. Near-field radiative transfer based thermal rectification using doped silicon. *Appl. Phys. Lett.* **98**, 113106 (2011).
21. Wang, L. P. & Zhang, Z. M. Thermal rectification enabled by near-field radiative heat transfer between intrinsic silicon and a dissimilar material. *Nanoscale Microscale Thermophys. Eng.* **17**, 337–348 (2013).
22. Yang, Y. *et al.* Radiation-based near-field thermal rectification with phase transition materials. *Appl. Phys. Lett.* **103**, 163101 (2013).
23. Ben-Abdallah, P. & Biehs, S. A. Phase-change radiative thermal diode. *Appl. Phys. Lett.* **103**, 191907 (2013).
24. Ito, K. *et al.* Experimental investigation of radiative thermal rectifier using vanadium dioxide. *Appl. Phys. Lett.* **105**, 253503 (2014).
25. Qazilbash, M. M. *et al.* Mott transition in VO₂ revealed by infrared spectroscopy and nano-imaging. *Science*. **318**, 1750–1753 (2007).
26. Barker, A. S. *et al.* Infrared optical properties of vanadium dioxide above and below the transition temperature. *Phys. Rev. Lett.* **17**, 1286 (1966).
27. Ben-Abdallah, P. & Biehs, S. A. Near-field thermal transistor. *Phys. Rev. Lett.* **112**, 044301 (2014).
28. Joulain, K. *et al.* Modulation and amplification of radiative far field heat transfer: Towards a simple radiative thermal transistor. *Appl. Phys. Lett.* **106**, 133505 (2015).
29. Prod'homme, H. *et al.* Optimized thermal amplification in a radiative transistor. *J. Appl. Phys.* **119**, 194502 (2016).
30. Ordóñez-Miranda, J. *et al.* Transistorlike Device for Heating and Cooling Based on the Thermal Hysteresis of VO₂. *Phys. Rev. Appl.* **6**, 054003 (2016).
31. Ordóñez-Miranda, J. *et al.* Dynamical heat transport amplification in a far-field thermal transistor of VO₂ excited with a laser of modulated intensity. *J. Appl. Phys.* **119**, 203105 (2016).
32. Xie, R. *et al.* An Electrically Tuned Solid-State Thermal Memory Based on Metal–Insulator Transition of Single-Crystalline VO₂ Nanobeams. *Adv. Funct. Mater.* **21**, 1602–1607 (2011).
33. Dumas-Bouchiat, *et al.* rf-microwave switches based on reversible semiconductor-metal transition of VO₂ thin films synthesized by pulsed-laser deposition. *Appl. Phys. Lett.* **91**, 223505 (2007).
34. Dumas-Bouchiat, *et al.* RF microwave switches based on reversible metal-semiconductor transition properties of VO₂ thin films: an attractive way to realise simple RF microelectronic devices. *MRS Online Proceedings Library Archive. Materials & Devices for Smart Systems III* **1129**, 275–286 (2009).
35. Wu, X. *et al.* Influence of thermal cycling on structural, optical and electrical properties of vanadium oxide thin films. *Appl. Surf. Sci.* **255**, 2840–2844 (2008).
36. Cao, J. *et al.* Thermoelectric Effect across the Metal–Insulator Domain Walls in VO₂ Microbeams. *Nano Lett.* **9**, 4001–4006 (2009).
37. Ramírez, J. G. *et al.* First-order reversal curve measurements of the metal-insulator transition in VO₂: Signatures of persistent metallic domains. *Phys. Rev. B*. **79**, 235110 (2009).
38. Kumar, S. *et al.* Electrical Switching in Semiconductor-Metal Self-Assembled VO₂ Disordered Metamaterial. *Coatings. Sci. Rep.* **6**, 37699 (2016).
39. Yang, T. H. *et al.* Semiconductor-metal transition characteristics of VO₂ thin films grown on c- and r-sapphire substrates. *J. Appl. Phys.* **107**, 053514 (2010).
40. Kucharsczyk, D. & Niklewski, T. Accurate X-ray determination of the lattice parameters and the thermal expansion coefficients of VO₂ near the transition temperature. *J. Appl. Crystallogr.* **12**, 370–373 (1979).
41. Oh, D. W. *et al.* Thermal conductivity and dynamic heat capacity across the metal-insulator transition in thin film VO₂. *Appl. Phys. Lett.* **96**, 151906 (2010).
42. Kizuka, H. *et al.* Temperature dependence of thermal conductivity of VO₂ thin films across metal–insulator transition. *Jpn. J. Appl. Phys.* **55**, 053201 (2015).
43. Kats, M. A. *et al.* Ultra-thin perfect absorber employing a tunable phase change material. *Appl. Phys. Lett.* **101**, 221101 (2012).
44. Kats, M. A. *et al.* Vanadium dioxide as a natural disordered metamaterial: perfect thermal emission and large broadband negative differential thermal emittance. *Phys. Rev. X*. **3**, 041004 (2013).
45. Guinneton, F. *et al.* Comparative study between nanocrystalline powder and thin film of vanadium dioxide VO₂: electrical and infrared properties. *J. Phys. Chem. Solid.* **62**, 1229–1238 (2001).
46. Leahu, G. *et al.* Anomalous optical switching and thermal hysteresis during semiconductor-metal phase transition of VO₂ films on Si substrate. *Appl. Phys. Lett.* **103**, 231114 (2013).
47. Voti, R. L. *et al.* Optimization of thermochromic VO₂ based structures with tunable thermal emissivity. *J. Appl. Phys.* **112**, 034305 (2012).
48. Saitzek, S. *et al.* VO₂ thin films deposited on silicon substrates from V2O5 target: Limits in optical switching properties and modeling. *Thin Solid Films*. **516**, 891–897 (2008).
49. Kim, M. *et al.* Substrate-mediated strain effect on the role of thermal heating and electric field on metal-insulator transition in vanadium dioxide nanobeams. *Sci. Rep.* **5**, 10861 (2015).
50. Guinneton, F. *et al.* Optimized infrared switching properties in thermochromic vanadium dioxide thin films: role of deposition process and microstructure. *Thin Solid Films*. **446**, 287–295 (2004).
51. Almond, D. P. and Patel, P. M. *Photothermal Science and Techniques in Physics and its Applications* (ed. Chapman & Hall) 7–28 (London, 1996).
52. Mandelis, A. & Zver, M. M. Theory of photopyroelectric spectroscopy of solids. *J. Appl. Phys.* **57**, 4421–4430 (1985).
53. Vanniasinkam, J. *et al.* Photopyroelectric deconvolution of bulk and surface optical-absorption and nonradiative energy conversion efficiency spectra in Ti:Al₂O₃. *J. Appl. Phys.* **75**, 8090–8097 (1994).
54. Ordóñez-Miranda, J. & Alvarado-Gil, J. J. Infrared emissivity determination using a thermal-wave resonant cavity: comparison between the length- and frequency-scan approaches. *Int. J. Therm. Sci.* **74**, 208–213 (2013).
55. Matvienko, A. and Mandelis, A. High-Precision and High-Resolution Measurements of Thermal Diffusivity and Infrared Emissivity of Water–Methanol Mixtures Using a Pyroelectric Thermal Wave Resonator Cavity: Frequency-Scan Approach. *Int. J. Thermophys.* **26**, 837–854 (2005).
56. Shen, J. *et al.* Signal generation mechanisms, intracavity-gas thermal-diffusivity temperature dependence, and absolute infrared emissivity measurements in a thermal-wave resonant cavity. *Rev. Sci. Instrum.* **69**, 197–203 (1998).
57. Shen, J. & Mandelis, A. Thermal-wave resonator cavity. *Rev. Sci. Instrum.* **66**, 4999–5005 (1995).
58. Forero-Sandoval, I. Y. *et al.* Study of thermal conductivity of magnetorheological fluids using the thermal-wave resonant cavity and its relationship with the viscosity. *Smart Mater. Struct.* **26**, 025010 (2016).
59. Vales-Pinzón, C. *et al.* Heat Transport in Liquid Polyester Resin with Carbon Nanotubes. *Int. J. Thermophys.* **36**, 2854–2861 (2015).

60. Shen, J. *et al.* Thermal-wave resonant-cavity measurements of the thermal diffusivity of air: a comparison between cavity-length and modulation-frequency scans. *Int. J. Thermophys.* **17**, 1241–1254 (1996).
61. Macias, J. *et al.* Photothermal Determination of Infrared Emissivity of Selective Solar Absorbing Coatings. *Int. J. Thermophys.* **36**, 1051–1056 (2015).
62. Choi, H. S. *et al.* Mid-infrared properties of a VO₂ film near the metal-insulator transition. *Phys. Rev. B.* **54**, 4621–4628 (1996).
63. Ito, K. *et al.* Multilevel radiative thermal memory realized by the hysteretic metal-insulator transition of vanadium dioxide. *Appl. Phys. Lett.* **108**, 053507 (2016).
64. Zerov, V. *et al.* Features of the operation of a bolometer based on a vanadium dioxide film in a temperature interval that includes a phase transition. *J. Opt. Technol.* **66**, 387 (1999).

Acknowledgements

This work has been partially supported by the Projects 192 “Fronteras de la ciencia”, 251882 “Investigación Científica Básica 2015” and the Cellule Énergie du CNRS through the grant N° 267745. C.L. Gomez-Heredia and J.A. Ramirez-Rincon thank Conacyt for their PhD scholarships as well as to the “Becas Mixtas” fund for supporting their stay at the Pprime Institute of the CNRS in France. Authors acknowledge the technical support of Hélène Grassin and Jose Bante Guerra for performing the emissivity experiments. X-ray diffraction and SEM analyzes were performed at the National Laboratory of Nano and Biomaterials (Funded by Fomix-Yucatán and Conacyt 2008–108160 Y), Cinvestav-IPN, Unidad Merida. We thank Dr. Patricia Quintana for allowing us to use the facilities of LANNBIO, M.C. Daniel Aguilar for his technical support in obtaining the diffractograms, and M.C. Dora Huerta and M.C Beatriz Heredia for their valuable assistance in the obtaining of SEM and AFM images.

Author Contributions

C.L. Gomez-Heredia and J.A. Ramirez-Rincon performed the emissivity experiments and wrote the main manuscript. C. Champeaux and F. Dumas-Bouchiat developed and analyzed the VO₂ samples. J.J. Alvarado-Gil and O. Ares designed and built the thermal wave resonant cavity. Y. Ezzahri and K. Joulain analyzed and interpreted the experimental data. J. Ordonez-Miranda developed the theoretical modeling and proposed the experiments.

Additional Information

Supplementary information accompanies this paper at <https://doi.org/10.1038/s41598-018-26687-9>.

Competing Interests: The authors declare no competing interests.

Publisher's note: Springer Nature remains neutral with regard to jurisdictional claims in published maps and institutional affiliations.



Open Access This article is licensed under a Creative Commons Attribution 4.0 International License, which permits use, sharing, adaptation, distribution and reproduction in any medium or format, as long as you give appropriate credit to the original author(s) and the source, provide a link to the Creative Commons license, and indicate if changes were made. The images or other third party material in this article are included in the article's Creative Commons license, unless indicated otherwise in a credit line to the material. If material is not included in the article's Creative Commons license and your intended use is not permitted by statutory regulation or exceeds the permitted use, you will need to obtain permission directly from the copyright holder. To view a copy of this license, visit <http://creativecommons.org/licenses/by/4.0/>.

© The Author(s) 2018